X-type antiferromagnetic stacking for spintronics

```
Shui-Sen Zhang, <sup>1,2,3</sup> Zi-An Wang, <sup>3,2</sup> Bo Li, <sup>4</sup> Yuan-Yuan Jiang, <sup>3,2</sup> Shu-Hui Zhang, <sup>5</sup> Rui-Chun Xiao, <sup>6</sup> Lan-Xin Liu, <sup>3,2</sup> X. Luo, <sup>3</sup> W. J. Lu, <sup>3</sup> Mingliang Tian, <sup>1,7</sup> Y. P. Sun, <sup>1,3,8</sup> Evgeny Y. Tsymbal, <sup>9,*</sup> Haifeng Du, <sup>1,6,†</sup> and Ding-Fu Shao<sup>3,‡</sup>
```

¹ Anhui Province Key Laboratory of Low-Energy Quantum Materials and Devices, High Magnetic Field Laboratory, HFIPS, Chinese Academy of Sciences, Hefei, Anhui 230031, China

² University of Science and Technology of China, Hefei 230026, China

³ Key Laboratory of Materials Physics, Institute of Solid State Physics, HFIPS, Chinese Academy of Sciences, Hefei 230031, China

⁴ Institute for Advanced Study, Tsinghua University, Beijing, 100084, China

⁵ College of Mathematics and Physics, Beijing University of Chemical Technology, Beijing 100029, China

⁶ Institute of Physical Science and Information Technology, Anhui University, Hefei 230601, China

⁷ School of Physics and Materials Science, Anhui University, Hefei 230601, China

⁸ Collaborative Innovation Center of Microstructures, Nanjing University, Nanjing 210093, China

⁹ Department of Physics and Astronomy & Nebraska Center for Materials and Nanoscience, University of Nebraska, Lincoln, Nebraska 68588-0299, USA

* tsymbal@unl.edu; † duhf@hmfl.ac.cn; † dfshao@issp.ac.cn

Physical phenomena in condensed matter normally arise from the collective effect of all atoms, while selectively addressing a lone atomic sublattice by external stimulus is elusive. The later functionality may, however, be useful for different applications due to a possible response being different from that occurring when the external stimulus affects the whole solid. Here, we introduce cross-chain antiferromagnets, where the stacking of two magnetic sublattices form a pattern of intersecting atomic chains, supportive to the sublattice selectivity. We dub this antiferromagnetic (AFM) stacking X-type and demonstrate that it reveals unique spin-dependent transport properties not present in conventional magnets. Based on high-throughput analyses and computations, we unveil three prototypes of X-type AFM stacking and identify 15 X-type AFM candidates. Using β -Fe₂PO₅ as a representative example, we predict the sublattice-selective spin-polarized transport driven by the X-type AFM stacking, where one magnetic sublattice is conducting, while the other is not. As a result, a spin torque can be exerted solely on a single sublattice, leading to unconventional ultrafast dynamics of the Néel vector capable of deterministic switching of the AFM order parameter. Our work uncovers a previously overlooked type of magnetic moment stacking and reveals sublattice-selective physical properties promising for high-performance spintronic applications.

The alignment of magnetic moments in magnetically ordered materials determines their physical properties. For example, ferromagnets have parallel-aligned magnetic moments producing net magnetization that can be controlled by an applied magnetic field and is responsible for various spin-dependent transport properties. In contrast, antiferromagnets have magnetic orderings with atomic moments compensating each other and resulting in zero net magnetization^{1,2}. Due to the obvious difficulties in addressing a single magnetic sublattice by common electric or magnetic means, antiferromagnets seem to be spin-independent, not much promising for applications³.

Despite this seemingly limiting constraint, a plethora of interesting and potentially useful properties of antiferromagnets has been discovered recently. Among them are spin currents, spin torques, and tunneling magnetoresistance effects^{4–18}—key phenomena of spintronics. These advances have been stimulated by symmetry-based analyses which helped, in particular, identify antiferromagnets with momentum-dependent spin polarizations,

including spin-split collinear antiferromagnets^{19–28}, dubbed altermagnets^{26,27}, and noncollinear antiferromagnets^{4,7,14–16}.

Although the discovered new properties make antiferromagnets potentially useful^{29,30}, much more exciting opportunities for new physics and spintronic applications would emerge if one of the magnetic sublattices in antiferromagnets could be selectively addressed by electric means. This yet elusive perspective could not, however, be derived based on the global symmetry of antiferromagnets that relates their macroscopic properties to the spin-dependent electronic structure in momentum space but requires a real space consideration of their magnetic sublattice stacking.

Here, we introduce a new type of collinear antiferromagnetic (AFM) stacking, where two magnetic sublattices form a pattern of intersecting atomic chains. The associated cross-chain antiferromagnets, which we dub X-type antiferromagnets, reveal unique spin-dependent transport properties not known in conventional magnets. Based on high-

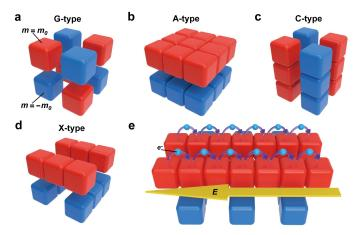


Fig. 1: "Building blocks" for antiferromagnets. (a) A G-type AFM stacking with the isolated magnetic moments aligned antiparallel between all nearest neighbors. (b) An A-type AFM stacking with the antiparallel-aligned FM layers. (c) A C-type AFM stacking with the antiparallel-aligned FM chains. (d) An X-type AFM stacking with the alternating layers of FM chains parallel to each other within the plane but crossing in the adjacent layers. (e) The sublattice selective spin transport allowed by the X-type AFM stacking.

throughput analyses and computations, we unveil three prototypes of X-type AFM stacking and identify 18 X-type AFM candidates. Using β -Fe₂PO₅ as a representative example, we predict that X-type AFM stacking supports sublattice-selective spin-dependent transport, where for a chosen transport direction, one magnetic sublattice is conducting, while the other is not. As a result of this unique property, a spin torque can be exerted solely on a single sublattice, leading to unconventional ultrafast dynamics of the Néel vector capable of deterministic switching of the AFM order parameter. Our results indicate the unprecedented opportunities for fundamental science and practical applications offered by the X-type AFM stacking.

Results

Conventional AFM stacking. Similar to ferromagnets and antiferromagnets being distinguished by their magnetic moment alignments, collinear antiferromagnets on their own are distinguished by different types of AFM stacking. In general, an antiferromagnet is a magnetically-ordered crystal characterized by three attributes: 1) equal magnitudes of magnetization of magnetic sublattices, $|\boldsymbol{m}_{\alpha}| = |\boldsymbol{m}_{\beta}|$, where α and β are sublattice indices; 2) vanishing net magnetization, $\boldsymbol{M} \propto \sum_{\alpha} \boldsymbol{m}_{\alpha} = 0$; and 3) a long-range AFM order, corresponding to a Heisenberg model with energy $H = -\sum_{\alpha \neq \beta} J_{\alpha\beta} \boldsymbol{m}_{\alpha} \boldsymbol{m}_{\beta}$ and a negative exchange parameter $J_{\alpha\beta} < 0$ between different sublattices. In collinear antiferromagnets, the two magnetic sublattices can have different structures and stacking patterns.

For example, Fig. 1 (a-c) illustrate typical G-, A-, and C-types of AFM stacking which have been originally proposed for simple cubic systems³¹, but now widely used to characterize a broad range of antiferromagnets. For a G-type antiferromagnet, basic "building blocks" are isolated magnetic moments aligned antiparallel between all nearest neighbors (Fig. 1(a)). In this sense, a G-type antiferromagnet can be considered as "genuine," due to AFM coupling solely controlling this type of stacking with ferromagnetic (FM) coupling playing a secondary role. On the contrary, for A-type or C-type antiferromagnets, where the building blocks are antiparallel-aligned two-dimensional (2D) FM-ordered layers (Fig. 1(b)) or one-dimensional (1D) FMordered atomic chains (Fig. 1(c)). Such a classification has been used over 70 years³¹ and involved other types of conventional AFM stacking such as D-, E-, and F-types, which represent mixtures of parallel and orthogonal FM-aligned chains (D and F) combined with isolated magnetic moments antiparallel to all their nearest neighbors (E).

The classification of AFM stacking is useful to derive sublattice dependent properties. As we discussed in our recent paper¹⁷, some AFM crystals exhibiting a C-type AFM stacking, e.g., those which belong to the rutile family, have small intrasublattice distances resulting in strong intra-sublattice electron hopping between the neighboring sites. A similar property is expected for certain A-type antiferromagnets. Therefore, from the electronic transport perspective, such A-type and C-type antiferromagnets qualitatively represent FM-ordered sublattices electrically connected in parallel. They support staggered Néel spin currents capable of driving spin-transfer torques and sizable TMR effects if used as electrodes in AFM tunnel junctions^{17,18}.

X-type AFM stacking. Antiferromagnets with stacking patterns other than mentioned above may exhibit even more exciting spin-dependent transport phenomena. As an example, let us consider 1D FM-ordered chains of atoms with opposite magnetic moment orientations (denoted as FMA and FMB) as the basic building blocks of a new type of AFM stacking. Instead of alternating FMA and FMB chains parallel to each other as in the C-type stacking, the new stacking order hosts alternating layers of FMA and FMB chains parallel to each other within the plane but crossing in the adjacent layers (Fig. 1(d)). Unlike the A-type AFM stacking with a similar FM ordering within the alternating planes, the new stacking has a sizable separation between the chains making them rather isolated in each plane. This does not violate the three above-mentioned attributes of the AFM order and thus should exist in nature. Due to FMA and FMB chain crossings in the antiferromagnets with such stacking, we dub as cross-chain antiferromagnets, antiferromagnets for short.

The proposed X-type AFM stacking is expected to reveal unconventional transport properties never discovered before.

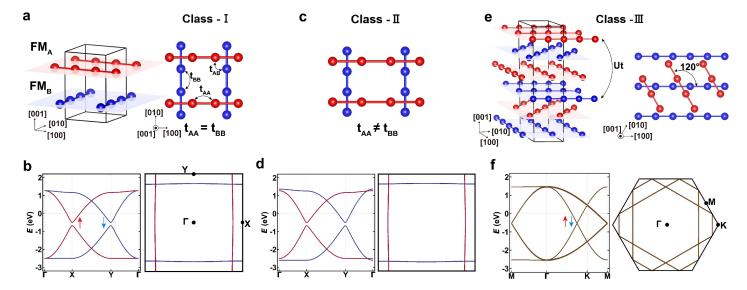


Fig. 2: Prototypes of X-type AFM Stacking. (a) The side view (left) and the top view (right) of the X-type AFM stacking of class-I, where the magnetic unit cell is the same as the crystal unit cell and the FM_A and FM_B chains are connected by crystal symmetry, leading to equal intra-chain hoppings. (b) The band structure with an altermagnetic spin splitting (left) and the associated Fermi surface (right) supported by the class-I X-type AFM stacking with $t_{AA} = t_{BB}$. (c) The top view of the X-type AFM stacking of class-II, where the magnetic unit cell is the same as the crystal unit cell, but the FM_A and FM_B chains are not connected by symmetry, leading to different intra-chain hoppings. (d) The band structure with a non-altermagnetic spin splitting (left) and the associated Fermi surface (right) supported by the class-II X-type AFM stacking with $t_{BB} = 1.05t_{AA}$. (e) The side view (left) and the top view (right) of the X-type AFM stacking of class-III, where the magnetic unit cell doubles the crystal unit cell resulting in the $\hat{U}\hat{t}$ symmetry combining spin rotation \hat{U} and half-unit-cell translation \hat{t} . (f) The spin degenerate band structure (left) and the Fermi surface (right) supported by the class-III X-type AFM stacking. In the calculations (b,d,f), we set $t_{AA} = 1$ eV, $t_{AB} = 0.3$ eV, $t_{AB} = 0.3$ eV, and t_{AB}

Due to the pronounced anisotropy associated with the two crosschain sublattices, X-type AFM metals are anticipated to exhibit strong anisotropy in their transport properties. For example, when applying an electric field along the FMA direction, the FMA chains are to be much more conductive for charge transport than the FM_B chains, provided by the strong intra-chain and weak inter-chain couplings (Fig. 1(e)). In addition, due to the chains being FM-ordered, the current flowing along the FMA chain must be spin-polarized. Therefore, unlike the A-type and C-type AFM stackings supporting staggered Néel spin currents on both sublattices, the X-type AFM stacking is expected to support isolated Néel spin currents selectively flowing along a single sublattice, provided that the two chains are orthogonal. Similarly, when applying an electric field along the FM_B direction, oppositely spin-polarized Néel spin currents appear in the FM_B chains, while the FMA chains become non-conducting.

Prototypes of X-type AFM stacking. Based on a high-throughput search within the dataset of Material Project³², we have identified more than 600 crystals composed of alternating layers of chains parallel to each other within the plane but

crossing in the adjacent layers. Assuming that the adjacent layers of chains are AFM-coupled in these cross-chain crystals, we identify three prototypes of the X-type AFM stacking order (Fig. 2). The first two prototypes, indicated as class-I and class-II, host the same magnetic unit cell as the crystal unit cell. They can be described by a minimum tight-binding toy model (Fig. 2(a,c)), as follows:

$$H = H_{AA} + H_{BB} + H_{AB}, (1)$$

where $H_{AA}(H_{BB})$ is the Hamiltonian of an isolated FM chain A(B), and H_{AB} is the coupling between FM chains A and B:

$$H_{AA} = t_{AA} \sum_{\alpha,\beta,\langle i,j\rangle} (c_{\alpha,i}^{\dagger} c_{\beta,j} + h.c.) - J \sum_{\alpha,i} c_{\alpha,i}^{\dagger} \boldsymbol{\sigma} \cdot \boldsymbol{m}_{\alpha} c_{\alpha,i}$$

$$+ \varepsilon_{0} \sum_{\alpha,i} c_{\alpha,i}^{\dagger} c_{\alpha,i},$$

$$H_{BB} = t_{BB} \sum_{\gamma,\delta,\langle i,j\rangle} (c_{\gamma,i}^{\dagger} c_{\delta,j} + h.c.) - J \sum_{\gamma,i} c_{\gamma,i}^{\dagger} \boldsymbol{\sigma} \cdot \boldsymbol{m}_{\gamma} c_{\gamma,i}$$

$$+ \varepsilon_{0} \sum_{\gamma,i} c_{\gamma,i}^{\dagger} c_{\gamma,i},$$

$$H_{AB} = t_{AB} \sum_{\alpha,\gamma,\langle i,j\rangle} (c_{\alpha,i}^{\dagger} c_{\gamma,j} + h.c.).$$
(2)

Here α, β (γ, δ) denote atomic sites within a unit cell of the FM_A (FM_B) chain, i (j) are cell indices, t_{AA} (t_{BB}) is intra-chain hopping parameter within the FM_A (FM_B) chain, t_{AB} is the hopping parameter between the FM_A and FM_B chains, J is the exchange parameter, ε_0 is the on-site energy, σ is the Pauli matrix vector, and $m_{\alpha}(m_{\gamma})$ is the magnetic moment on the sites $\alpha(\gamma)$.

Within the X-type AFM stacking order of class-I, FM_A and FM_B are connected by a symmetry operation \hat{O} or $\hat{T}\hat{O}$, where \hat{O} is a crystal symmetry such as a mirror/glide plane \hat{M}_{\parallel} perpendicular to the *x-y* plane, a two-fold rotation/screw axis $\hat{C}_{2\parallel}$ parallel to the *x-y* plane, or a four-fold screw axis \hat{C}_{4z} around the *z* direction, and \hat{T} is time reversal (Fig. 2(a)). These symmetries require $t_{AA} = t_{BB}$. This prototype of the X-type AFM stacking hosts an altermagnetic spin splitting (Fig. 2(b)).

The X-type AFM stacking order of class-II, on the other hand, does not have symmetry connection between FM_A and FM_B, due to different intra-chain/inter-chain distances or relative rotations/distortions of the structural motifs of the chains (Fig. 2(c)). This leads to a slightly different t_{AA} and t_{BB} . In this case, the spin degeneracy at the Γ point is removed (Fig. 2(d)), indicating a non-altermagnetic spin splitting, as was discussed recently³³.

We note that the momentum-dependent spin splitting can be understood based on the X-type AFM stacking in real space. For example, for X-type antiferromagnets with orthogonal crosschains (Fig. 2(a,c)) where the inter-chain hopping t_{AB} is not strong, the in-plane electron hopping is confined within the chain. Therefore, the two spin polarized bands contributed by FM_A (FM_B) are highly dispersive with a crossing in the Γ -X (Γ -Y) direction, but weakly dispersive with a large gap between the Γ -Y (Γ -X) direction, resulting in one-dimensional spin-polarized sheets (Fig. 2(b,d)). This band structure indicates that it can be qualitatively considered as the superposition of the electronic structures of the isolated FM_A (FM_B) chains.

In addition, there is an X-type AFM stacking order of class-III where the magnetic unit cell doubles the crystal unit cell, leading to the $\hat{U}\hat{t}$ symmetry combining spin rotation \hat{U} and half-unit-cell translation \hat{t} and compensating the magnetization (Fig. 2(e)). This prototype is spin-degenerate in the nonrelativistic limit, as shown in our model Hamiltonian calculation by introducing additional terms in Eq. (1) coming from the isolated chains and their coupling (Fig. 2(f)). The crystal structures supporting the class-III stacking can be found in trigonal and hexagonal systems where the adjacent cross-chains are connected by symmetry $\hat{T}\hat{C}_{3z}$ combining \hat{T} and three-fold screw axis \hat{C}_{3z} (Fig. 2(e)). Similar to class-I and class-II stackings, their band structures feature flat bands and band crossings (Fig. 2(f)). The class-III stacking also exhibits the sublattice/chain selectivity: by applying an electric field perpendicular to two

Table 1: Material candidates with X-type AFM stacking: chemical formula, spin space group, Material Project ID (MP-ID)³¹, and prototype class.

Chemical formula	Spin Space group	MP-ID	Prototype
Fe ₂ PO ₅ ³³	C-12/-1c [∞] m1	mp-553913	
Co ₂ PO ₅	$C^{-1}2/^{-1}c^{\infty}{}^{m}1$	mp-1272384	
KVAsO534	$P^{1}n^{-1}a^{-1}2_{1}^{\infty m}1$	mp-1202651	
KVPO535	$P^{1}n^{-1}a^{-1}2_{1}^{\infty m}1$	mp-19517	
$SrV_2(PO5)_2^{36}$	$F^{\text{-}1}d^{1}d^{\text{-}1}2^{^{\varpi}m}1$	mp-559580	
CaNi ₂ (PO ₅) ₂	$F^{-1}d^{-1}d^{1}d^{\infty m}1$	mp-1378551	
Al(FeO ₂) ₂	$I^{\text{-}1}4_{1}/{}^{1}a^{^{\varpi}m}1$	mp-1248448	Class-I
$VPbO_2$	$I^{\text{-}1}4_{\text{1}}/^{\text{1}}a^{^{\infty}m}1$	mp-1208173	
$Y(FeO_2)_2$	$I^{\text{-}1}4_{\text{1}}/^{\text{1}}a^{^{\infty}m}1$	mp-1405822	
$Ca(CoO_2)_2$	$I^{\text{-}1}4_{1}/^{1}a^{1}m^{\text{-}1}d^{^{\infty}m}1$	mp-1406903	
$\text{Co}_2\text{PO}_5^{37}$	$I^{\text{-}1}4_{\text{1}}/^{\text{1}}a^{\text{1}}m^{\text{-}1}d^{^{\infty}m}1$	mp-1105140	
$Fe_2PO_5^{39,40}$	$I^{\text{-}1}4_{1}/^{1}a^{1}m^{\text{-}1}d^{^{\infty}m}1$	mp-18830	
$VBiO_2$	$I^{\text{-}1}4_{1}/^{1}a^{1}m^{\text{-}1}d^{^{\infty}m}1$	mp-1207870	
SrV ₂ (PO ₅) ₂	P¹1 [∞] m1	mp-723593	Class-II
Co ₂ PO ₅	$I^l m^l m^l d^{^{\varpi}m} 1$	mp-1276873	

antiparallel chains in the cell, the staggered Néel spin currents can be selectively generated in the chains oblique to the electric field.

By calculating the exchange parameters of cross-chain materials based on 3d transition metals, we identify 15 X-type AFM candidates; among them 13 belong to class-I and 2 belong to class-II, with 6 being experimentally available^{34–40} as listed in Table 1 together with their spin space group^{41–43}. We point out that more X-type antiferromagnets can be further designed, including these that belong to class-III, by suitable element doping/substitution of cross-chain crystals in material dataset. Below, we consider the class-I X-type AFM candidate β -Fe₂PO₅^{39,40} as a representative example to demonstrate the sublattice-selective spin transport.

X-type AFM candidate β -**Fe₂PO₅.** Collinear antiferromagnet Fe₂PO₅ has been discovered more than 30 years ago^{39,40,44} but remains not widely known. It has two polymorphs, where the α -phase, which has an orthogonal unit cell and a C-type AFM stacking below 250K⁴⁴, and β -phase represents an X-type AFM stacking^{39,40}. Fig. 3(a) shows the crystal and magnetic structures of β -Fe₂PO₅, where the Fe atoms with upward and downward magnetic moments represent two magnetic sublattices denoted as Fe_A and Fe_B, respectively. The atomic structure of β -Fe₂PO₅ contains in-plane chains of face-sharing FeO₆ octahedra along the [100] and [010] directions of the tetragonal cell, which can be transformed to each other by the $\hat{T}\hat{C}_{4z}$ symmetry

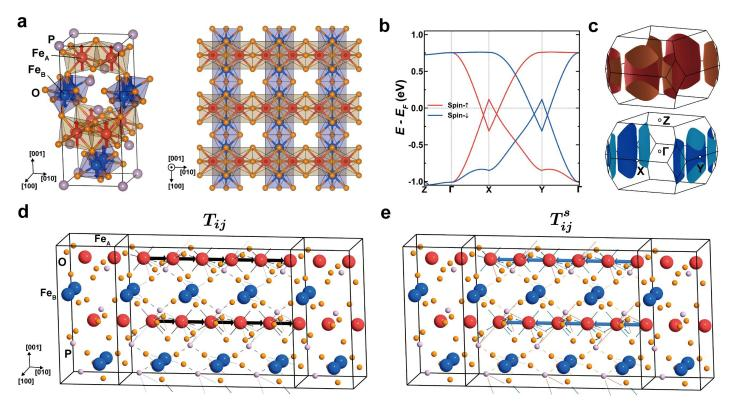


Fig. 3: X-type antiferromagnet β -Fe₂PO₅. (a) *Left*: Crystal and magnetic structures of β -Fe₂PO₅. Arrows denote the magnetic moments of Fe atoms. *Right*: Top view of two bottom layers in the unit cell shown in the left. P atoms are ignored. (b) Band structure of β -Fe₂PO₅. (c) The up-spin (top) and down-spin (bottom) Fermi surfaces of β -Fe₂PO₅. (d,e) Visualization of the calculated bond transmissions T_{ij} (d) and bond spin transmissions T_{ij}^{s} (e) of β -Fe₂PO₅. The directions of arrows indicate sign of $T_{ij}^{(s)}$ between atoms i and j, i.e. a rightward (leftward) arrow imply $T_{ij}^{(s)}$ being positive (negative). The width of the arrows is proportional to $\sqrt{|T_{ij}^{(s)}|}$.

transformation, indicating a class-I X-type AFM stacking. The P atoms are located between these chains. The Fe ions have a mixed 2+/3+ valence and a small Fe-Fe intra-chain distance, favoring an intra-chain FM coupling via the double-exchange interaction⁴⁵. These intersecting chains share common corners of the FeO₆ octahedra. The resulting Fe-O-Fe bond angle is ~125°, leading to a super-exchange interaction that favors the interchain AFM coupling⁴⁶. With a [001] directional Néel vector, β -Fe₂PO₅ belongs to the magnetic space group I4₁'/am'd. A monoclinic distortion of β -Fe₂PO₅ reported at low temperature³⁴ does not influence the X-type AFM stacking. The uniqueness of the X-type AFM stacking, metallic ground state, and the Néel temperature $T_N = 408 \text{ K}^{39,40}$ well above room temperature make β -Fe₂PO₅ interesting both for fundamental studies and for practical applications.

We perform first-principles DFT calculations⁴⁷ to explore the electronic and transport properties of β -Fe₂PO₅. Fig. 3(b,c) show the calculated nonrelativistic band structure and Fermi surface of β -Fe₂PO₅ that reveal giant altermagnetic spin

splitting⁴⁸ similar to that derived from our toy model (Fig. 2(b)). To elucidate spin-dependent transport properties, we calculate bond transmission $T_{ij} = T_{ij}^{\uparrow} + T_{ij}^{\downarrow}$ and bond spin transmission $T_{ij}^s = T_{ij}^{\uparrow} - T_{ij}^{\downarrow}$ for transport along the [010] direction, where \uparrow and \downarrow denote the two spin channels, and i and j are the atomic indices⁴⁹. As is evident from Fig. 3(d,e), these quantities reflect the anticipated chain-selective transport: both T_{ij} and T_{ij}^{s} are dominated by the Fe_A-Fe_A intra-chain bonds. It is notable that T_{ij}^s are negative, i.e., the spin current is flowing in the opposite direction to the charge current. This is due to the double-exchange interaction between FeA2+ and FeA3+ ions, which is mostly mediated by the hopping of electrons with the spins opposite to the Fe_A moments. As a result, the down-spin bands along the Γ -Y direction are highly dispersive (Fig. 3(b)), leading to the down-spin Fermi sheets representative to 1D transmission along the [010] direction (Fig. 3(c)). On the other hand, although there are mobile up-spin electrons on the FeB chains to mediate the intra-chain double-exchange interaction, the weak inter-chain coupling due to the large Fe_A-Fe_B and Fe_B-

Fe_B inter-chain distances leads to negligible T_{ij} and T_{ij}^{s} associated with Fe_B. Therefore, the dispersions of the up-spin bands are weak and have a large energy gap in the Γ-Y direction (Fig. 3(b)). The transport spin polarization in this case is estimated to be as high as ~68% in the ballistic regime, which is further enhanced to ~94% in the diffusive regime, due to a small $T_{ij}^{(s)}$ associated with Fe_B being scattered out⁴⁷. Similarly, for transport along the [100] direction, the total transmission is majorly contributed by the hopping of up-spin electrons between intra-chain Fe_B atoms, corresponding to the band structure along the Γ-X direction and leading the up-spin Fermi surface sheets (Fig. 3(b,c)). Therefore, the spin-split electronic structure of β-Fe₂PO₅ can be qualitatively considered as the superposition of the electronic structures of the isolated Fe_A and Fe_B chains, as expected based on our toy model.

The strong intra-chain spin transmission supports highly spin-polarized Néel spin currents along the chains in β -Fe₂PO₅. These Néel spin currents are highly anisotropic due to the X-type AFM stacking. For example, an electric field along the [110] direction produces crossing Néel spin currents with opposite spin polarizations along the Fe_A and Fe_B chains. These currents can be decomposed into a transverse global spin current and the staggered longitudinal Néel spin current hidden in a globally spin-neutral current. On the other hand, when the electric field is along one of the chain directions ([100] or [010]), only the longitudinal chains are conductive producing an isolated Néel spin current, while the transverse chains are almost insulating.

Spin torques on a single sublattice. The robust sublattice selective spin-dependent transport property is very interesting, as it opens a possibility to realize the sublattice-resolved spintronic phenomena. As an example, we show that X-type antiferromagnets, such as β -Fe₂PO₅, allow exerting a spin torque on a single magnetic sublattice. This can be achieved by passing an external spin current along one of the FM-chain directions or by using an isolated Néel spin current on one type of FM chains in the presence of asymmetric boundary conditions to generate self-torque. Assuming that the current is flowing along the FM_A sublattice with magnetic moments m_A pointing to the +z direction, the associated magnetic dynamics of an X-type antiferromagnet can be described by the Landau-Lifshitz-Gilbert-Slonczewski equations^{50,51}:

$$\dot{\boldsymbol{m}}_{A} = \boldsymbol{\tau}_{A}^{F} + \boldsymbol{\tau}_{A}^{D} + \boldsymbol{\tau}_{A}^{FL} + \boldsymbol{\tau}_{A}^{DL},$$

$$\dot{\boldsymbol{m}}_{B} = \boldsymbol{\tau}_{B}^{F} + \boldsymbol{\tau}_{B}^{D}.$$
(3)

Here $\boldsymbol{\tau}_{\alpha}^{F} \propto -\boldsymbol{m}_{\alpha} \times \boldsymbol{H}_{eff,\alpha}$ and $\boldsymbol{\tau}_{\alpha}^{D} \propto \boldsymbol{m}_{\alpha} \times \dot{\boldsymbol{m}}_{\alpha} = -\boldsymbol{m}_{\alpha} \times (\boldsymbol{m}_{\alpha} \times \boldsymbol{H}_{eff,\alpha})$ are the precession and damping torques on sublattice α induced by the intrinsic effective field $\boldsymbol{H}_{eff,\alpha}$, respectively, and $\boldsymbol{\tau}_{A}^{FL} \propto -\boldsymbol{m}_{A} \times \boldsymbol{H}_{st}$ and $\boldsymbol{\tau}_{A}^{DL} \propto -\boldsymbol{m}_{A} \times (\boldsymbol{m}_{A} \times \boldsymbol{H}_{st})$ are the field-like and damping-like torques driven by a

spin-torque effective field \mathbf{H}_{st} oriented toward the -z direction. Since $H_{eff,\alpha}$ includes the anisotropy field $H_{K,\alpha}$ and the exchange field $\pmb{H}_{E,\alpha}$, the $\pmb{ au}_{lpha}^F$ and $\pmb{ au}_{lpha}^D$ can be further decomposed as $\boldsymbol{\tau}_{\alpha}^F = \boldsymbol{\tau}_{K,\alpha}^F + \boldsymbol{\tau}_{E,\alpha}^F$ and $\boldsymbol{\tau}_{\alpha}^D = \boldsymbol{\tau}_{K,\alpha}^D + \boldsymbol{\tau}_{E,\alpha}^D$, where the subscripts K and E denote the associated torques driven by $\mathbf{H}_{K,\alpha}$ and $\mathbf{H}_{E,\alpha}$, respectively. Due to $H_{E,\alpha}$ being much larger than $H_{K,\alpha}$, $\tau_{\alpha}^F \approx$ $\boldsymbol{\tau}_{E,\alpha}^F$ and $\boldsymbol{\tau}_{\alpha}^D \approx \boldsymbol{\tau}_{E,\alpha}^D$ when \boldsymbol{m}_A and \boldsymbol{m}_B are not perfectly antiparallel. Fig. 4(a,b) schematically show how these torques affect the dynamics of m_A and m_B . When the isolated spintorque carrying effective field H_{st} is applied solely to m_A , the associated damping-like torque au_A^{DL} pulls $extbf{ extit{m}}_A$ away from the easy-axis toward the -z direction. This creates canting between m_A and m_B , and hence $H_{E,\alpha}$ exerts non-zero torques τ_{α}^F and τ_{α}^D on both moments ${m m}_A$ and ${m m}_B$. The torque ${m au}_{lpha}^F$ generates oscillations of the Néel vector, while the torque $\boldsymbol{\tau}_B^D$ pulls \boldsymbol{m}_B toward +z direction even without assistance of an external spin torque. Using realistic parameters $|\mathbf{H}_{K,\alpha}| = 2 \text{ T}, |\mathbf{H}_{E,\alpha}| = 100$ T, and the damping factor of 0.01, we find that \mathbf{H}_{st} much smaller than $H_{K,\alpha}$ (0.17 $|H_{K,\alpha}| < |H_{st}| < 0.24 |H_{K,\alpha}|$) is sufficient to switch the Néel vector (Fig. 4(c)). The switching trajectory is similar to that for the spin-transfer torque in ferromagnets^{50,51}, indicating the decisive role of the damping-like torque τ_A^{DL} . Since this H_{st} can be driven by an external spin current, the AFM domains can be aligned according to the spin polarization of the external spin source. This solves the challenging problem of AFM spintronics where measurable time-reversal-odd properties (e.g., TMR in AFM tunnel junctions) are strongly diminished by misaligned domains.

Interestingly, we find that a larger H_{st} ($|H_{st}| > 0.24 |H_{K,\alpha}|$) can drive ultrafast oscillations of the Néel vector (Fig. 4(d)). This is because of the much stronger canting of m_A and m_B that produces a large out-of-plane component of τ_A^F competing with τ_A^{DL} . This property distinguishes the dynamics of X-type antiferromagnets from other antiferromagnets, where full switching and ultrafast oscillations cannot be generated using the same type of spin torques^{9,10,52}.

Discussion

Among the 18 antiferromagnets with the X-type AFM stacking we identified, 12 are metallic and hence are expected to support the properties discussed in this work. For the remaining 6 insulating X-type antiferromagnets, the sublattice selective transport properties associated with magnon excitations are possible⁵³, offering promising opportunities for spintronics with low-energy dissipation and long coherence length.

In addition to the existing X-type antiferromagnets, the X-type AFM stacking may occur in magnets which are not natural antiferromagnets. For example, one can design *X-type ferrimagnets*, with AFM stacking of cross-chains composed of

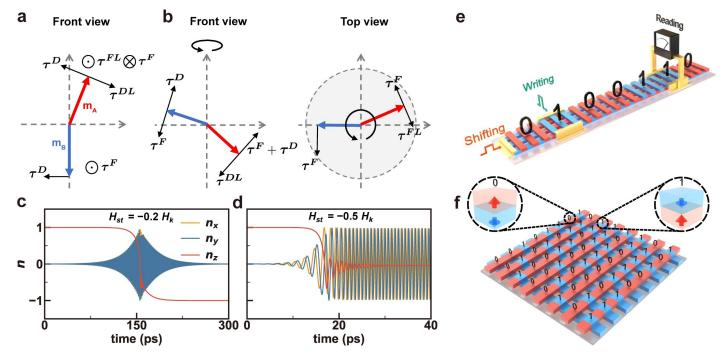


Fig. 4: Sublattice selective spin torques and their implications for spintronics. (a) Vectors of magnetic moments and spin torques in the initial process of spin dynamics. (b) Vectors of magnetic moments and spin torques in the process of Néel vector oscillations driven by the single-sublattice spin torque: front (left) and top (right) views. (c,d) Simulated dynamics of the x, y, and z components of the normalized Néel vector \mathbf{n} under the current-induced spin-torque effective field $H_{st} = -0.2H_K$ (c) and $H_{st} = -0.5H_K$ (d). (e) Schematic of an X-type racetrack memory. Here, the colored bars denote FM_A and FM_B chains of an X-type antiferromagnet, where the upward (downward) magnetic moments are denoted by red (blue) color. In this schematic, we assume with a slight exaggeration that the electrodes contact three chains. (f) Schematic of the X-type AFM stacking with crossing atomic chains forming an intrinsic crossbar array. Each bar is composed of a bunch of parallel chains, and the red and blue colors denote upward and downward moment orientations in these chains. The gaps between these bars are the chains not connected to the electrodes. The AFM domains at the intersections of these bars represent "0" and "1" bits.

different magnetic elements. In addition, it is possible to engineer *synthetic* X-type antiferromagnets with the same advantages as their natural counterparts.

From the technological point of view, the X-type AFM stacking offers a new approach for non-volatile memories. For example, in an X-type antiferromagnet, one can selectively nucleate and move domains via spin torques by passing an isolated Néel spin current or an external spin current along a chosen FM_A or FM_B chain (Fig. 4(e)). This promises an ultrafast X-type racetrack memory, where the oppositely magnetized AFM domains can serve as "0" and "1" bits of information (Fig. 4(e)). Moreover, the X-type AFM stacking with crossing chains of magnetic atoms forms an intrinsic crossbar array that is widely used in magnetic random-access memories (MRAMs) (Fig. 4(f)). Assuming a bilayer array of β -Fe₂PO₅ with one bit area containing a domain of 50×50 intersecting chains, the

associated storage density is ~15 Tb/in², promising for future big data applications.

Overall, the X-type AFM stacking signifies an exciting field of research for fundamental science and an attractive new paradigm for AFM spintronics. The predicted sublattice-selective electronic transport carrying isolated Néel spin currents has multiple important implications, such as spin torques exerted on a single magnetic sublattice, unconventional ultrafast spin dynamics, and deterministic switching of the AFM domains. These unprecedented functionalities promise new AFM spintronic devices which can be employed in non-volatile memories with ultra-high density and ultra-fast switching speed. We hope therefore that our theoretical results will stimulate the experimentalists working in this field to explore the properties of X-type AFM stacking relevant to spintronics and beyond.

Acknowledgments

This work was supported by the National Key R&D Program of China (Grant No. 2021YFA1600200), the National Natural Science Funds for Distinguished Young Scholar (Grant No. 52325105), the National Natural Science Foundation of China (Grants Nos. 12274411, 12241405, and 52250418), the Basic Research Program of the Chinese Academy of Sciences Based on Major Scientific Infrastructures (Grant No. JZHKYPT-2021-08), and the CAS Project for Young Scientists in Basic Research (Grant No. YSBR-084). E.Y.T acknowledges support from the Division of Materials Research of the National Science Foundation (NSF grant No. DMR-2316665). Computations were performed at Hefei Advanced Computing Center.

REFERENCES

- Néel, L. Propriétés magnétiques du manganèse et du chrome en solution solide etendue. J. Phys. Radium 3, 160 (1932).
- 2. Néel, L. Antiferromagnetism and Ferrimagnetism. *Proc. Phys. Soc. A* **65**, 869–885 (1952).
- 3. Nobel Foundation. *Nobel Lectures Physics: Including Presentation Speeches and Laureates' Biographies. 1963-1970.* vol. 4 (Elsevier Pub. Co. for the Nobel Foundation, Amsterdam, 1972).
- 4. Železný, J., Zhang, Y., Felser, C. & Yan, B. Spin-Polarized Current in Noncollinear Antiferromagnets. *Phys. Rev. Lett.* **119**, 187204 (2017).
- 5. Naka, M. *et al.* Spin current generation in organic antiferromagnets. *Nat Commun* **10**, 4305 (2019).
- González-Hernández, R. et al. Efficient Electrical Spin Splitter Based on Nonrelativistic Collinear Antiferromagnetism. Phys. Rev. Lett. 126, 127701 (2021).
- 7. Gurung, G., Shao, D.-F. & Tsymbal, E. Y. Transport spin polarization of noncollinear antiferromagnetic antiperovskites. *Phys. Rev. Mater.* **5**, 124411 (2021).
- 8. Ma, H.-Y. *et al.* Multifunctional antiferromagnetic materials with giant piezomagnetism and noncollinear spin current. *Nat Commun* **12**, 2846 (2021).
- Železný, J. et al. Relativistic Néel-Order Fields Induced by Electrical Current in Antiferromagnets. Phys. Rev. Lett. 113, 157201 (2014).
- 10. Manchon, A. *et al.* Current-induced spin-orbit torques in ferromagnetic and antiferromagnetic systems. *Rev. Mod. Phys.* **91**, 035004 (2019).
- 11. Wadley, P. *et al.* Electrical switching of an antiferromagnet. *Science* **351**, 587–590 (2016).

- 12. Shao, D.-F., Zhang, S.-H., Li, M., Eom, C.-B. & Tsymbal, E. Y. Spin-neutral currents for spintronics. *Nat Commun* **12**, 7061 (2021).
- Šmejkal, L., Hellenes, A. B., González-Hernández, R., Sinova, J. & Jungwirth, T. Giant and Tunneling Magnetoresistance in Unconventional Collinear Antiferromagnets with Nonrelativistic Spin-Momentum Coupling. *Phys. Rev. X* 12, 011028 (2022).
- 14. Dong, J. *et al.* Tunneling Magnetoresistance in Noncollinear Antiferromagnetic Tunnel Junctions. *Phys. Rev. Lett.* **128**, 197201 (2022).
- 15. Qin, P. *et al.* Room-temperature magnetoresistance in an all-antiferromagnetic tunnel junction. *Nature* **613**, 485–489 (2023).
- 16. Chen, X. *et al.* Octupole-driven magnetoresistance in an antiferromagnetic tunnel junction. *Nature* **613**, 490–495 (2023).
- 17. Shao, D.-F. *et al.* Néel Spin Currents in Antiferromagnets. *Phys. Rev. Lett.* **130**, 216702 (2023).
- 18. Shao, D.-F. & Tsymbal, E. Y. Antiferromagnetic tunnel junctions for spintronics. *npj Spintronics* **2**, 1–13 (2024).
- 19. Wu, C., Sun, K., Fradkin, E. & Zhang, S.-C. Fermi liquid instabilities in the spin channel. *Phys. Rev. B* **75**, 115103 (2007).
- 20. Hayami, S., Yanagi, Y. & Kusunose, H. Momentum-Dependent Spin Splitting by Collinear Antiferromagnetic Ordering. *J. Phys. Soc. Jpn.* **88**, 123702 (2019).
- 21. Yuan, L.-D., Wang, Z., Luo, J.-W., Rashba, E. I. & Zunger, A. Giant momentum-dependent spin splitting in centrosymmetric low- Z antiferromagnets. *Phys. Rev. B* **102**, 014422 (2020).
- 22. Yuan, L.-D., Wang, Z., Luo, J.-W. & Zunger, A. Prediction of low-Z collinear and noncollinear antiferromagnetic compounds having momentum-dependent spin splitting even without spin-orbit coupling. *Phys. Rev. Mater.* 5, 014409 (2021).
- 23. Hayami, S., Yanagi, Y. & Kusunose, H. Bottom-up design of spin-split and reshaped electronic band structures in antiferromagnets without spin-orbit coupling: procedure on the basis of augmented multipoles. *Phys. Rev. B* **102**, 144441 (2020).
- Liu, P., Li, J., Han, J., Wan, X. & Liu, Q. Spin-Group Symmetry in Magnetic Materials with Negligible Spin-Orbit Coupling. *Phys. Rev. X* 12, 021016 (2022).
- Mazin, I. I., Koepernik, K., Johannes, M. D., González-Hernández, R. & Šmejkal, L. Prediction of unconventional magnetism in doped FeSb2. *Proc. Natl. Acad. Sci.* 118, e2108924118 (2021).
- Šmejkal, L., Sinova, J. & Jungwirth, T. Beyond Conventional Ferromagnetism and Antiferromagnetism: A

- Phase with Nonrelativistic Spin and Crystal Rotation Symmetry. *Phys. Rev. X* **12**, 031042 (2022).
- 27. Šmejkal, L., Sinova, J. & Jungwirth, T. Emerging Research Landscape of Altermagnetism. *Phys. Rev. X* **12**, 040501 (2022).
- 28. Yuan, L.-D. & Zunger, A. Degeneracy Removal of Spin Bands in Collinear Antiferromagnets with Non-Interconvertible Spin-Structure Motif Pair. *Adv. Mater.* **35**, 2211966 (2023).
- 29. Jungwirth, T., Marti, X., Wadley, P. & Wunderlich, J. Antiferromagnetic spintronics. *Nat. Nanotechnol.* **11**, 231–241 (2016).
- 30. Baltz, V. et al. Antiferromagnetic spintronics. Rev. Mod. Phys. 90, 015005 (2018).
- 31. Wollan, E. O. & Koehler, W. C. Neutron Diffraction Study of the Magnetic Properties of the Series of Perovskite-Type Compounds [(1-x)La, xCa]MnO₃. *Phys. Rev.* **100**, 545–563 (1955).
- 32. Jain, A. *et al.* Commentary: The Materials Project: A materials genome approach to accelerating materials innovation. *APL Materials* **1**, 011002 (2013).
- 33. Yuan, L.-D. Nonrelativistic spin splitting at the Brillouin zone center in compensated magnets. *Phys. Rev. Lett.* **133**, 216701 (2024).
- 34. Elkaim, E. *et al.* Occurrence of a monoclinic distortion in beta-Fe₂PO₅. *Acta Cryst B* **52**, 428–431 (1996).
- 35. Belkhiri, S., Mezaoui, D. & Roisnel, T. K₂V₂O₂(AsO₄)₂. *Acta Cryst E* **68**, i54–i54 (2012).
- Benhamada, L., Grandin, A., Borel, M. M., Leclaire, A. & Raveau, B. KVPO₅, an intersecting tunnel structure closely related to the hexagonal tungsten bronze. *Acta Cryst C* 47, 1138–1141 (1991).
- 37. Berrah, F., Leclaire, A., Borel, M.-M., Guesdon, A. & Raveau, B. A new vanadium(IV) monophosphate, Sr(VO)₂(PO₄)₂, isotypic with Ca(VO)₂(PO₄)₂. *Acta Cryst C* 55, 288–291 (1999).
- 38. Wang, G., Valldor, M., Spielberg, E. T. & Mudring, A.-V. Ionothermal Synthesis, Crystal Structure, and Magnetic Study of Co₂PO₄OH Isostructural with Caminite. *Inorg. Chem.* **53**, 3072–3077 (2014).
- 39. Ech-Chahed, B., Jeannot, F., Malaman, B. & Gleitzer, C. Pre'paration ete'tude d'une varie'te'basse tempe'rature de l'oxyphosphate de fer de valence mixte βFe2(PO4)O et de NiCr(PO4)O: Un cas d'e'changee'lectronique rapide. *J. Solid State Chem* **74**, 47–59 (1988).
- 40. Ijjaali, M., Mallaman, B. & Gleitzer, C. Stability, Structure Refinement, and Magnetic Properties of beta-Fe₂PO₅. *J. Solid State Chem* **86**, 195–205 (1990).

- 41. Xiao, Z., Zhao, J., Li, Y., Shindou, R. & Song, Z.-D. Spin Space Groups: Full Classification and Applications. *Phys. Rev. X* **14**, 031037 (2024).
- 42. Chen, X. *et al.* Enumeration and Representation Theory of Spin Space Groups. *Phys. Rev. X* **14**, 031038 (2024).
- 43. Jiang, Y. *et al.* Enumeration of Spin-Space Groups: Toward a Complete Description of Symmetries of Magnetic Orders. *Phys. Rev. X* **14**, 031039 (2024).
- Warner, J., Cheetham, A., Cox, D. & Vondreele, R. Valence contrast between iron sites in alpha-Fe2PO5 a comparative-study by magnetic neutron and resonant x-ray-powder diffraction. *J Am Chem Soc* 114, 6074–6080 (1992).
- Zener, C. Interaction between the d-Shells in the Transition Metals. II. Ferromagnetic Compounds of Manganese with Perovskite Structure. *Phys. Rev.* 82, 403–405 (1951).
- 46. Anderson, P. W. Antiferromagnetism. Theory of Superexchange Interaction. *Phys. Rev.* **79**, 350–356 (1950).
- 47. See Supplemental Material.
- 48. He, T. *et al.* Topological nodal lines and nodal points in the antiferromagnetic material beta-Fe₂PO₅. *J. Mater. Chem. C* 7, 12657–12663 (2019).
- Solomon, G. C., Herrmann, C., Hansen, T., Mujica, V. & Ratner, M. A. Exploring local currents in molecular junctions. *Nature Chem* 2, 223–228 (2010).
- 50. Slonczewski, J. C. Current-driven excitation of magnetic multilayers. *J. Magn. Magn. Mater.* **159**, L1–L7 (1996).
- 51. Zhang, S., Levy, P. M. & Fert, A. Mechanisms of spin-polarized current-driven magnetization switching. *Phys. Rev. Lett.* **88**, 236601 (2002).
- 52. Cheng, R., Daniels, M. W., Zhu, J.-G. & Xiao, D. Ultrafast switching of antiferromagnets via spin-transfer torque. *Phys. Rev. B* **91**, 064423 (2015).
- Z.-A. Wang, B. Li, S.-S. Zhang, W.-J. Lu, M. Tian, Y.-P. Sun, E. Y. Tsymbal, K. Wang, H. Du, and D.-F Shao, Giant uncompensated magnon spin currents in X-type magnets, arXiv:2502.13511 (2025).